SCIENTIFIC REPORTS

OPEN

SUBJECT AREAS:
BATTERIES
NANOPARTICLES

Received
14 May 2014

Accepted
11 August 2014

Published
25 September 2014

Correspondence and requests for materials should be addressed to J.C. (chenabc@nankai.edu.cn)

* These authors contributed equally to this work.

Ultrasmall Li_2S Nanoparticles Anchored in Graphene Nanosheets for High-Energy Lithium-Ion Batteries

Kai Zhang*, Lijiang Wang*, Zhe Hu, Fangyi Cheng & Jun Chen

Key Laboratory of Advanced Energy Materials Chemistry (Ministry of Education), Collaborative Innovation Center of Chemical Science and Engineering, Chemistry College, Nankai University, Tianjin 300071, China.

Li_2S has a high theoretical capacity of 1166 mAh g^{-1}, but it suffers from limited rate and cycling performance. Herein we reported in-situ synthesis of thermally exfoliated graphene−Li_2S (in-situ TG−Li_2S) nanocomposite and its application as a superior cathode material alternative to sulfur. Li_2S nanoparticles with the size of ~8.5 nm homogeneously anchored in graphene nanosheets were prepared via chemical reduction of pre-sublimed sulfur by lithium triethylborohydride ($LiEt_3BH$). The in-situ TG−Li_2S nanocomposite exhibited an initial capacity of 1119 mAh g^{-1} Li_2S (1609 mAh g^{-1} S) with a negligible charged potential barrier in the first cycle. The discharge capacity retained 791 mAh g^{-1} Li_2S (1137 mAh g^{-1} S) after 100 cycles at 0.1C and exceeded 560 mAh g^{-1} Li_2S (805 mAh g^{-1} S) at a high rate of 2C. Moreover, coupling the composite with Si thin film anode, a Li_2S/Si full cell was produced, delivering a high specific capacity of ~900 mAh g^{-1} Li_2S (1294 mAh g^{-1} S). The outstanding electrode performance of in-situ TG−Li_2S composite was attributed to the well dispersed small Li_2S nanoparticles and highly conductive graphene nanosheets, which provided merits of facile ionic and electronic transport, efficient utilization of the active material, and flexible accommodation of volume change.

There is an increasing demand in developing high-energy, safe, and cheap cathode materials of rechargeable lithium batteries for various mobile applications such as consumer electronics and electric vehicles. Sulfur has been proposed as an attractive candidate due to the advantages of high theoretical capacity (1675 mAh g^{-1}), natural abundance, low cost, and environmental friendliness[1]. Nevertheless, sulfur electrode is plagued by its low electronic conductivity, large volume change during charge-discharge processes, and severe dissolution of intermediate high-order polysulfides in organic electrolyte[2]. In addition, safety problems arise from the formation of Li dendrite on the anode surface. To address these issues, many efforts have been proposed, including encapsulating sulfur in carbon materials and/or conducting polymers[3–7] and the use of ethers electrolyte with additives (e.g., $LiNO_3$ and polysulfides), "Solvent in Salt" electrolyte, or short-chain S_{2-4}[8–10]. Recently, Li_2S has attracted particular interest as an alternative cathode material[11–16]. The Li_2S cathode has a theoretical specific capacity of 1166 mAh g^{-1} and can be combined with lithium-free high-capacity anode (e.g., Si and Sn)[17,18]. Moreover, the damage of volumetric contraction to Li_2S electrode is less than expansion of sulfur electrode during the first cycle[19,20]. Similar to the sulfur cathode, Li_2S is also hampered by low electronic conductivity (~10^{-13} S cm^{-1}) and polysulfides shuttle phenomenon[21]. Furthermore, the potential barrier during the first charge process leads to a utilized capacity penalty[19]. Attempts to enhance the conductivity include composing Li_2S with a conductive matrix such as CMK-3, microporous carbon, graphite, graphene oxide, and polypyrrole[14–17,20,22]. Setting a higher charging cutoff potential can compulsively activate Li_2S, while reducing the particle size and improving the dispersion of Li_2S are demonstrated to alleviate the potential barrier[13,23]. Not surprisingly, downsizing Li_2S particles and loading Li_2S on a conductive matrix can lead to faster electrode kinetics[24–26], which benefits the efficient utilization of the active materials and the better accommodation of large volume change[27,28]. For preparation of Li_2S nanoparticles, ball-milling bulk Li_2S and reducing S-containing precursors have been reported[13,22]. However, the formation of ultrafine Li_2S nanoparticles (<10 nm) uniformly dispersed in conductive matrix remains challenging.

In this study, we report the electrochemical application of in-situ thermally exfoliated graphene−Li_2S nanocomposite (denote as in-situ TG−Li_2S) with ultrasmall Li_2S nanoparticles (~8.5 nm) in graphene nanosheets. The thermally exfoliated graphene (TG) is employed to load S via a melt-diffusion method to form TG−S composite, which is then chemically lithiated with lithium triethylborohydride ($LiEt_3BH$) to form uniformly

dispersed Li_2S nanoparticles. Owing to the unique architecture, the as-synthesized in-situ TG−Li_2S nanocomposite exhibits remarkably enhanced electrode performance including higher capacity, better rate capability, superior cyclability, and reduced potential barrier, as compared to the counterpart ex-situ TG−supported commercial Li_2S powder (denote as ex-situ TG−Li_2S). To take advantage of the high-capacity Li_2S, we have also assembled and investigated Li_2S/Si full cells coupling the in-situ TG−Li_2S nanocomposite cathode with Si thin film anode. The results indicate that the in-situ TG−Li_2S nanocomposite is a promising material for rechargeable lithium-ion batteries.

Results

Figure 1a shows the X-ray diffraction (XRD) patterns of the TG and three composite samples (i.e., TG−S, in-situ TG−Li_2S, and ex-situ TG−Li_2S). The diffraction peaks of TG−S are similar to that of TG and no sulfur peak is observed, which indicates that sulfur is diffused inside the pores of TG[29]. Compared to the profiles of TG−S, the pattern of the in-situ TG−Li_2S sample indicates the formation of Li_2S, but the characteristic peaks of Li_2S are very weak and broad. From the thermal analysis curve of in-situ TG−Li_2S composite (Figure S1), the weight gain of 60 wt.% is due to the formation of Li_2SO_4, which is detected by XRD analysis after heat treatment at 600°C. The Li_2S content is determined to be 67 wt.% with the detailed calculation described in the caption of Figure S1. The ex-situ TG−Li_2S composite including the same Li_2S content displays much more intensive and sharper peaks of Li_2S. The results suggest that Li_2S in the in-situ TG−Li_2S composite has a better dispersive state and a smaller particle size than that in the ex-situ TG−Li_2S sample. Raman spectra (Figure 1b) were also measured to characterize the prepared samples. Two peaks centered at 1345 and 1590 cm^{-1} can be respectively assigned to the D band of disordered carbon and the G band of graphitic carbon in the graphene matrix[29]. For the TG−S composite, two weak peaks are found at 218 and 471 cm^{-1}, which proves the presence of sulfur[30]. The Raman signals of S completely disappear after chemical reduction. The peak (370 cm^{-1}, induced by the stretching vibration of Li−S bond[21]) assigned to Li_2S is not observed for the in-situ TG−Li_2S, whereas it is clearly visible for the ex-situ TG−Li_2S. This difference indicates that the Li_2S particles are well impregnated inside the pores of TG for the in-situ composite.

The texture of the as-prepared samples was analyzed by N_2 adsorption-desorption measurement. As shown in Figure 1c, the pristine TG displays a high Brunauer−Emmett−Teller (BET) surface area of 552.0 $m^2 g^{-1}$. After impregnating sulfur, the BET surface area is decreased to 50.9 $m^2 g^{-1}$. The corresponding pore volume is also reduced from 3.11 $cm^3 g^{-1}$ to 0.20 $cm^3 g^{-1}$ (Figure S2). However, for the in-situ TG−Li_2S composite, the porous structure almost disappears based on its much lower BET surface area (4.7 $m^2 g^{-1}$) and pore volume (0.02 $cm^3 g^{-1}$). The results also confirm that the pores of TG are filled by Li_2S in the in-situ TG−Li_2S composite.

Figures 2a–c display the scanning electron microscope (SEM) images of TG, TG−S, and in-situ TG−Li_2S. The pristine TG shows crumpled laminar structure with abundant pores surrounded by thin graphene nanosheets (Figure 2a). For both TG−S (Figure 2b) and in-situ TG−Li_2S (Figure 2c), the crumpled laminar structure is maintained; however, the corrugation greatly decreases and the laminar thickness gradually increases as compared to the pristine TG. The surface of TG in the ex-situ TG−Li_2S composite is entirely covered by Li_2S and the crumpled laminar structure completely disappears (Figure S3). The energy-dispersive X-ray (EDX) elemental mapping of the in-situ TG−Li_2S indicates that Li_2S is homogenously dispersed in the TG matrix (Figures 2d–f).

The crumpled structure of TG before and after loading S is further confirmed by the TEM images of the TG and TG−S composite (Figure S4). After lithiation, the Li_2S nanoparticles with average particle size of ~8.5 nm are found (Figures 2g–i). The crystal planes (111) of Li_2S with d-spacing of 0.32 nm is clearly seen in the HRTEM images (Figure 2h). On the other hand, seriously agglomerated Li_2S particles are detected in the ex-situ TG−Li_2S composite (Figure S5). The formation of the homogeneously dispersed ultrasmall Li_2S particles is attributed to the solution method and the porous structure of graphene[31].

The electrochemical performance of the in-situ and ex-situ TG−Li_2S composites was monitored using coin cells. The two cathodes both contain ~53 wt.% Li_2S (i.e., 44 wt.% S) with an area loading of ~1.3 mg Li_2S/cm^2. Figure 3a shows the first charge-discharge curves of the two composites. The in-situ TG−Li_2S composite dis-

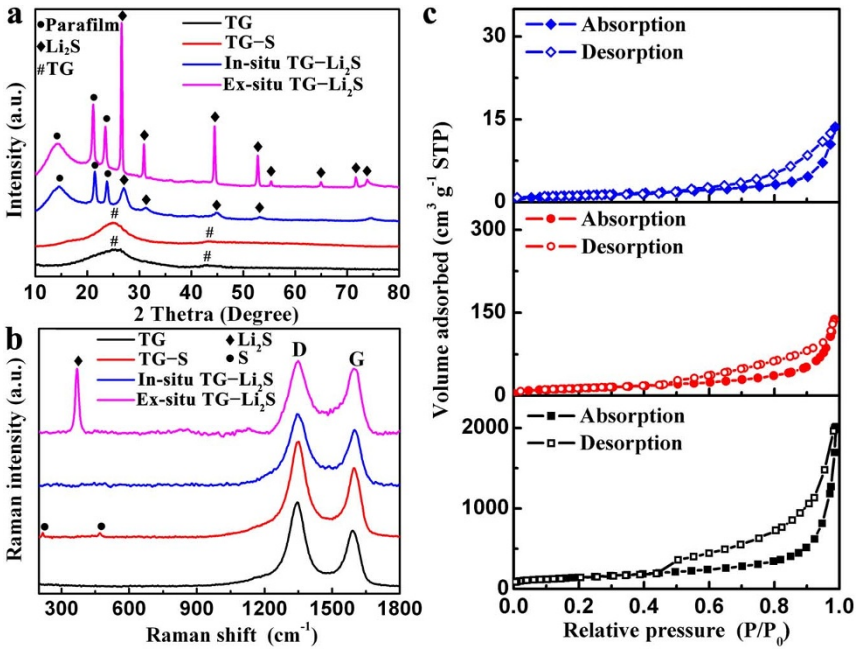

Figure 1 | (a) XRD patterns and (b) Raman spectra of the pristine TG and three composites (TG−S, in-situ TG−Li_2S, and ex-situ TG-Li_2S). Parafilm is used to prevent the contact between Li_2S and H_2O. (c) N_2 adsorption-desorption isotherms of TG, TG−S, and in-situ TG−Li_2S.

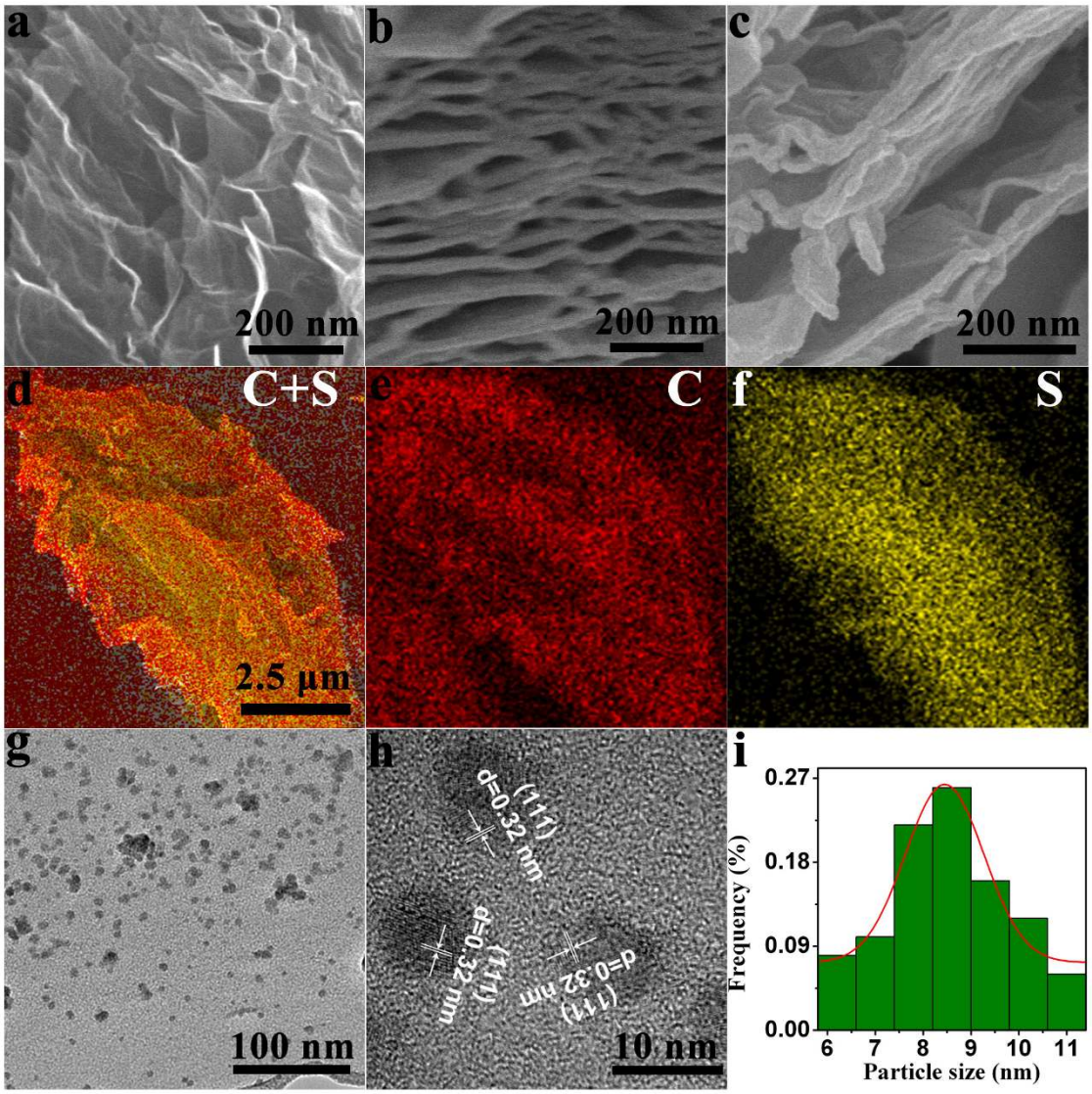

Figure 2 | Scanning electron microscopy (SEM) images of the pristine TG (a), TG−S composite (b), and in-situ TG−Li_2S composite (c). (d–f) Energy-dispersive X-ray (EDX) elemental mappings of carbon (red) and sulfur (yellow) for the in-situ TG−Li_2S. Transmission electron microscopy (TEM) (g) and high-resolution TEM (HRTEM) (h) images and particle distribution curve (i) of the in-situ TG−Li_2S composite.

plays a plateau at about 2.5 V with almost invisible potential barrier during the first charge process. For the ex-situ TG−Li_2S, there is an apparent potential barrier in the charge process, which suggests a sluggish activation process[19]. The potential barrier and charge overpotential increase with the current rate (Figure S6). Notably, for the in-situ TG−Li_2S composite, Li_2S can be activated at a higher rate and a lower cutoff potential, which is desirable to increase the energy efficiency. The discharge behaviors of the in-situ and ex-situ TG−Li_2S composites are similar, but the in-situ TG−Li_2S composite exhibits higher discharge plateaus.

Figure 3b displays the second charge-discharge curves. The in-situ TG−Li_2S composite also exhibits higher discharge plateaus and lower charge plateaus than those of the ex-situ TG−Li_2S composite, while the latter holds obvious charge overpotential. Figure 3c shows the typical cyclic voltammograms (CVs) of the in-situ and ex-situ TG−Li_2S composites. Both composites reveal two cathodic peaks and two anodic peaks that match the redox reactions of sulfur/Li_2S_x and Li_2S_x/Li_2S couples, but the redox peaks of the in-situ TG−Li_2S composite are sharper and more symmetrical. In addition, the in-situ TG−Li_2S has a lower polarization.

The cycling performance of the in-situ and ex-situ TG−Li_2S composites was evaluated at a rate of 0.1C. As shown in Figure 3d, the in-situ TG−Li_2S composite delivers a high discharge capacity of 1119 mAh g^{-1} Li_2S (equivalent to 1609 mAh g^{-1} S) in the first cycle, while the value for the ex-situ TG−Li_2S composite is only 933 mAh g^{-1} Li_2S (1341 mAh g^{-1} S). Table S1 lists the discharge capacities at different cycles for the two composites. After 100 cycles, the remained capacities of the in-situ and ex-situ TG−Li_2S composites are 791 mAh g^{-1} Li_2S (1137 mAh g^{-1} S) and 452 mAh g^{-1} Li_2S (650 mAh g^{-1} S), respectively, corresponding to capacity retentions of 83% and 59%. Notably, for the in-situ TG−Li_2S composite, the average capacity loss is only 0.8 mAh g^{-1} Li_2S per cycle from the 10th to the 100th cycle and the Coulombic efficiency is also higher than that of the ex-situ TG−Li_2S composite. Furthermore, the electrolyte additives are also very important to improve the performance. The cell with both polysulfide and $LiNO_3$ additives delivers better stability and higher capacity (Figure S7). We have also attempted to increase the Li_2S loading. The electrode composed of 95 wt.% in-situ TG−Li_2S composite and 5 wt.% binder was also tested. In this case, the higher Li_2S or S mass ratio (64 wt.% Li_2S or 55 wt.% S) causes a slight decrease of initial capacity and cycling performance; the discharge capacity remains ~600 mAh g^{-1} Li_2S (862 mAh g^{-1} S) after 100 cycles at 0.1C (Figure S8).

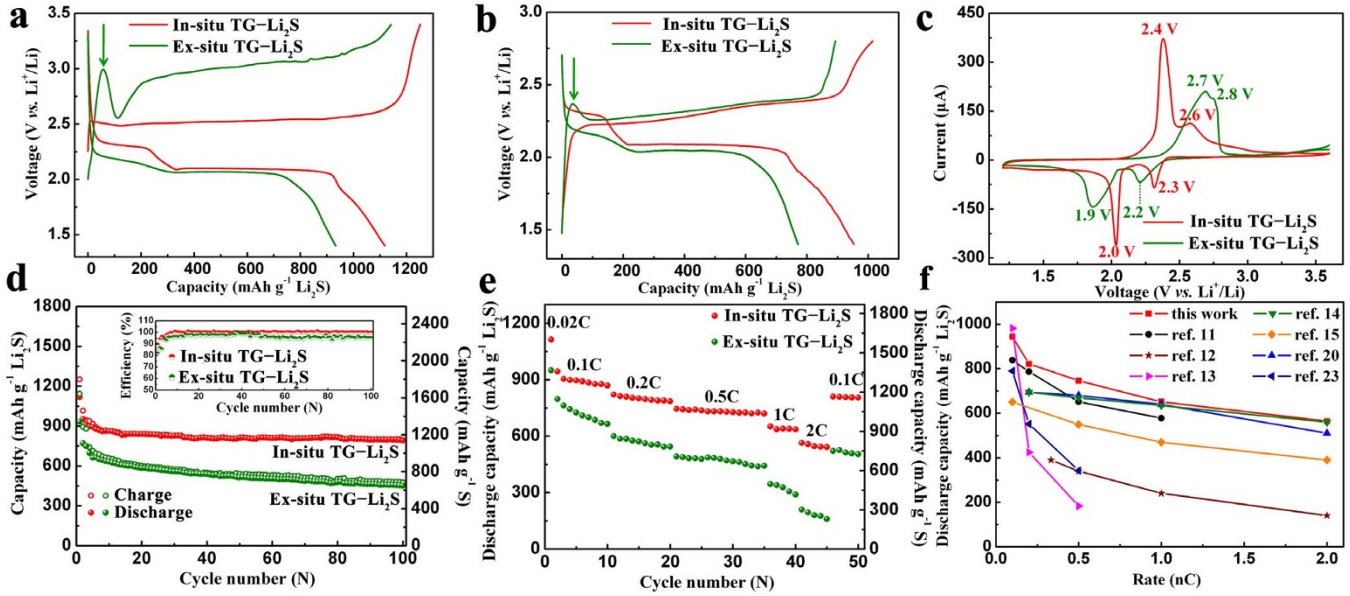

Figure 3 | The first (a) and second (b) charge-discharge curves, (c) cyclic voltammograms (CVs) at the scan rate of 0.1 mV s^{-1}, (d) cycling performance with Coulombic efficiency (inset), and (e) rate capability of the in-situ and ex-situ TG−Li_2S composites. (f) Comparison of the rate performance among reported Li_2S cathodes. For in-situ TG−Li_2S cathode, the mass ratio of in-situ TG−Li_2S composite: conductive carbon: binder is 8 : 1 : 1, with loading of ~53 wt.% Li_2S and ~1.3 mg Li_2S/cm^2. For ex-situ TG−Li_2S cathode, the mass ratio of Li_2S powder: TG: conductive carbon: binder is 53 : 27 : 10 : 10.

The rate performance of the in-situ and ex-situ TG−Li_2S composites is also compared in Figure 3e. As the current rate increases from 0.1 to 1C, the discharge capacity of the in-situ TG−Li_2S composite slightly decreases. Even at a high rate of 2C, the composite sustains a high discharge capacity of 565 mAh g^{-1} Li_2S (812 mAh g^{-1} S), which is an outstanding performance for Li_2S cathode (Figure 3f). When the current density recovers to 0.1C, the capacity regains 811 mAh g^{-1} Li_2S (1166 mAh g^{-1} S). But for the ex-situ TG−Li_2S composite, the discharge capacity is only 492 mAh g^{-1} Li_2S (707 mAh g^{-1} S) at 0.5C, which is even lower than that of the in-situ TG−Li_2S composite at 2C.

Electrochemical impedance spectroscopy (EIS) was employed to analyze the kinetics of electrochemical reactions. Figures 4a and 4b show EIS of the in-situ and ex-situ TG−Li_2S composites tested after 10 cycles at different discharge states (i. e., medium potential at each discharge plateau). All curves include a semicircle in the high frequency region and a straight line in the low frequency region. The semicircle can be assigned to the charge transfer resistance (R_{ct}) and the straight line relates to ionic diffusion. At the same discharge state, the in-situ TG−Li_2S composite shows lower R_{ct}, which is attributed to the favorable dispersed state and ultrasmall particle size of Li_2S. The apparent activation energies (E_a) of electrochemical reactions can be calculated by the following equations[32–34],

$$i_0 = RT/nFR_{ct} \quad (1)$$

$$i_0 = A\exp(-E_a/RT) \quad (2)$$

where i_0 is the exchange current, A is the temperature-independent coefficient, R is the gas constant, T is the absolute temperature, n is the number of transferred electrons, and F is the Faraday constant. Figures 4c and 4d display the Arrhenius plots of $\ln(T/R_{ct})$ versus 1000/T for the in-situ and ex-situ TG−Li_2S composites at different discharge states. The corresponding EIS curves are shown in Figure S9. The calculated E_a is 52.4 kJ mol^{-1} at 2.30 V and 59.3 kJ mol^{-1} at 2.09 V for the in-situ TG−Li_2S composite, while the two values for the ex-situ TG−Li_2S composite are 70.3 kJ mol^{-1} at 2.16 V and 72.2 kJ mol^{-1} at 2.05 V, respectively. The lower activation energy of the in-situ TG−Li_2S composite indicates enhanced kinetics of the electrochemical reactions.

The remarkable performance of half cell motivates us to further investigate its application in full cell. We coupled the Li_2S cathode with a high-capacity thin film Si anode (Figure S10), which can deliver a specific capacity of 1841 mAh g^{-1} and a good cycling performance (Figure S11). Figure 5a schematically shows the composition of the Li_2S/Si full cell. This cell contains a theoretical 2Li-storage cathode and a 4.4Li-storage anode, along with the same electrolyte used for the half cell. The Li_2S/Si full cell gives discharge capacities of 900, 733, and 526 mAh g^{-1} Li_2S (i.e., 1294, 1054, and 756 mAh g^{-1} S) at rates of 0.05, 0.2, and 1C, respectively (Figure 5b). There are one charge plateau with negligible barrier and two discharge plateaus in the first cycle (Figure 5c). For the second cycle, the discharge plateaus are similar but the charge plateau becomes slopping. The average discharge voltages are 1.7 V at 0.05C and 1.6 V at 1C. Table S2 compares the Li_2S/Si cell with other full cell systems. The fabricated Li_2S/Si cell in this paper exhibits a higher specific capacity than those of reported Li_2S-based full cells and traditional Li-ion batteries[17,23,35–37], indicating its promising application as advanced energy-storage batteries.

Discussion

The above results indicate that the in-situ TG−Li_2S composite exhibits negligible potential barrier, high capacity, high-rate capability, and long-term cycling stability. The relief of the potential barrier is attributed to the homogeneously dispersed ultrasmall Li_2S nanoparticles and the TG matrix with high electronic conductivity. In the first charge process, Li_2S losses Li^+ ions to form deficient $Li_{2-x}S$ until the voltage reaches the top of the barrier. Then, $Li_{2-x}S$ is slowly transformed to high-order lithium polysulfides (Li_2S_y, $4 \leq y \leq 8$), which gradually delithiate to form S_8[19]. The potential barrier represents the sluggish kinetics of the formation of polysulfides. The ultrafine Li_2S particles embedded in graphene nanosheets benefit the enhancement of kinetics and the full utilization of the active materials.

The superior electrode performance is also attributed to the ultrasmall size of Li_2S nanoparticles and the porous structure of TG. The

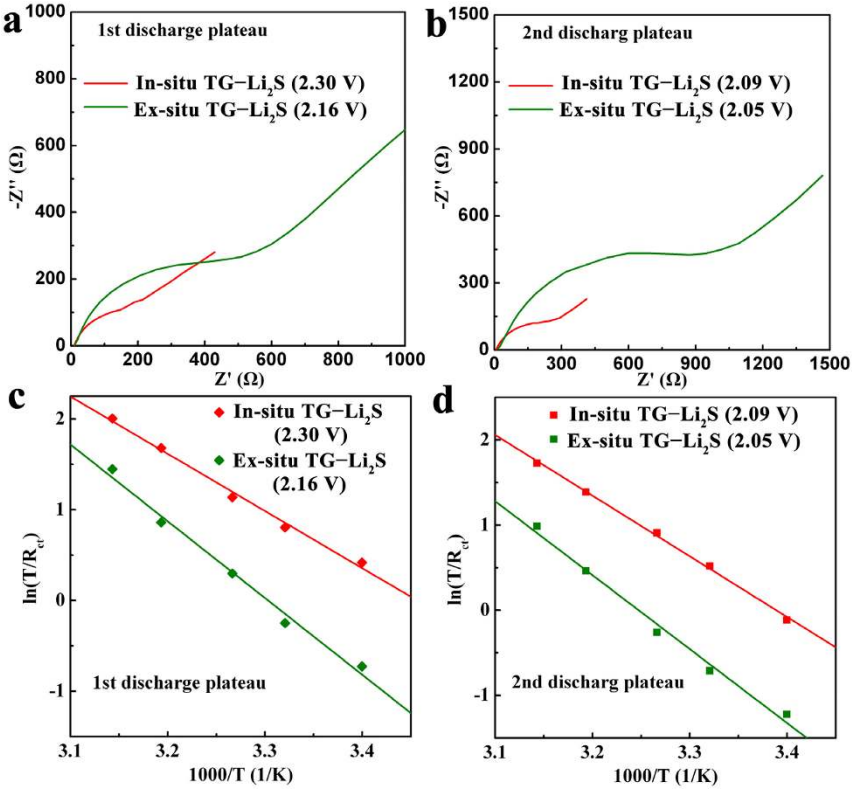

Figure 4 | **Electrochemical impedance spectroscopy (EIS) (a, b) and Arrhenius plots of ln(T/R_{ct}) versus 1000/T (c, d) of the in-situ and ex-situ TG−Li_2S composites at different discharge states (medium potential at each discharge plateau) tested after 10 cycles.**

ultrasmall Li_2S nanoparticles facilitate the accommodation of the volume change on cycling and the reduction of ionic diffusion length, leading to little polarization. Also, the porous structure of the TG matrix inhibits the dissolution of polysulfides, and its high electronic conductivity effectively improves the electronic transport, which enhances the Coulombic efficiency, cycling stability, and rate performance. Last, the electrolyte additives are also very important to improve the capacity retention and Coulombic efficiency. As is well known, $LiNO_3$ facilitates the formation of passivation film on the surface of lithium metal, which suppresses the formation of lithium dendrites and significantly relieves the capacity fading[3]. Polysulfide additive is also used to compensate for the loss of active material from the electrode[19].

In summary, we have prepared nanostructured in-situ TG−Li_2S composite through chemical lithiation of the TG−S composite using $LiEt_3BH$. The in-situ TG−Li_2S composite delivered an initial discharge capacity of 1119 mAh g^{-1} and almost invisible potential barrier in the first cycle as well as excellent long-period cyclability and high-rate capability (2C, 565 mAh g^{-1}) owing to the synergistic effect from the excellent physical properties of TG, ultrasmall Li_2S nanoparticles (~8.5 nm), and optimization of the electrolyte. The Li_2S/Si full cell coupling the in-situ TG−Li_2S composite cathode and the Si thin film anode exhibited a high discharge capacity of 900 mAh g^{-1} at 0.05C. The Li_2S/Si full cell offers considerable application potential toward the development of high-energy rechargeable batteries.

Methods

Preparation of the thermally exfoliated graphene nanosheet (TG), TG−S, and in-situ TG−Li_2S samples. The graphene oxide (GO) is prepared via a Staudenmaier method[38]. Details of the synthesis procedures can be found in Supporting Information. The GO was heated to 1000°C in a crucible under Ar atmosphere for 2 h with a heating rate of 5°C min^{-1}. 50 mg of the as-prepared exfoliated graphene (TG) was mixed with 175 mg of sulfur and the mixture was ground for 30 min in an agate mortar. The above sample was heated to 155°C for 12 h. Then, the temperature was

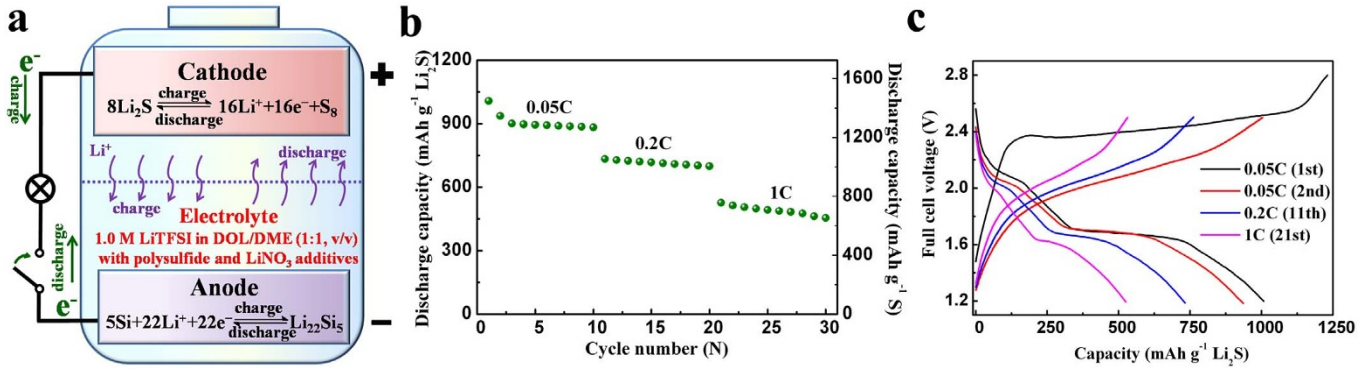

Figure 5 | (a) Schematic of the structure of the fabricated Li_2S/Si full cell with the corresponding electrode reactions. (b) Capacity retention of the Li_2S/Si full cell sequentially cycled at 0.05, 0.2, and 1C, and (c) the corresponding charge-discharge curves at different cycles.

raised to 250°C for 2 h to clear away the sulfur over the outside surface of TG under Ar protection. Finally, lithium triethylborohydride ($LiEt_3BH$) in tetrahydrofuran (THF) solution was added to the as-prepared TG−S in an argon-filled glove box and the obtained suspension was vacuum evaporated at 110°C for 10 h to remove all the liquid.

Material characterization. X-ray powder diffraction (XRD) patterns were recorded on a Rigaku MiniFlex600 with Cu K_α radiation in the 2θ range from 3° to 80°. Raman spectra were collected using a confocal Raman microscope (DXR, Thermo-Fisher Scientific) with a 532 nm from an argon-ion laser. The morphology of the as-prepared samples was observed using scanning electron microscopy (SEM, JEOL, JSM-7500F) and transmission electron microscopy (TEM, tecnai G2 F20) with an energy dispersive X-ray spectrometer (EDS). The N_2 adsorption-desorption analysis was measured at 77 K on a BELSORP-mini instrument. Thermal analysis was carried out on NETZSCH STA 449F thermal analyzer (Germany), in which the samples were heated under O_2 flow to 800°C at a heating rate of 5°C min^{-1}.

Electrochemical Tests. The working electrode was prepared from a mixture of 80 wt.% of the active materials (in-situ TG−Li_2S), 10 wt.% of carbon nanotubes (CNTs) and 10 wt.% of the polyvinylidene fluoride (PVdF) binder in N-methyl-2-pyrrolidone (NMP). The obtained slurry was also spread on an Al current collector and then dried in a vacuum oven at 110°C for 6 h to remove the solvent completely. For comparison, ex-situ TG−Li_2S composite was prepared by a dispersion–deposition process: 53 wt.% commercial Li_2S powder and 27 wt.% graphene were first added in NMP and stirred for 4 h to form a homogenous slurry, and then 10 wt.% PVdF and 10 wt.% of CNTs in NMP solution was mixed into the above slurry under continuous stirring. The obtained slurry was also spread on an Al current collector and then dried in a vacuum oven at 110°C for 4 h. Lithium metal was used as the anode and reference electrode. The separator was Cellgard 2320. The electrolyte was 1.0 M lithium bis(trifluoromethanesulfonyl)imide (LiTFSI) in a mixture of 1,3-dioxolane (DOL) and 1,2-dimethoxyethane (DME) (1 : 1, v/v) with polysulfide and $LiNO_3$ additives. A 1.0 M LiTFSI solution, a 0.2 M $LiNO_3$ solution, and a polysulfide ([S] = 0.5 M) solution were mixed together at a volume ratio of 25 : 25 : 1. A 80 μL of as-prepared electrolyte (containing ~0.025 mg S) was added in the cell and the sulfur content in the Li_2S electrode is ~1.0 mg. The amount of S in polysulfide additive is only 2.5% of that in the cathode. The polysulfide additive contributed little to the total capacity, so the specific capacity was calculated excluding the mass of polysulfide additive for clarity. The CR2032 coin-type cells were fabricated in an argon-filled glove box (Mikrouna Universal 2440/750). In full cells, the Si thin film prepared by sputter method was used instead of lithium metal and its mass was ~1.5 times that of Li_2S. The assembled cells were tested on a CT2001A cell test instrument (LAND Electronic Co.). Electrochemical impedance spectroscopy (EIS) measurements were conducted on Parstat 2273 electrochemical workstation (AMETEK Company). The ac perturbation signal was ±5 mV and the frequency range was from 10 mHz to 100 KHz. The cyclic voltammograms (CV) were performed at a scan rate of 0.1 $mV \cdot s^{-1}$ with a Parstat 263A electrochemical workstation (AMTECT Company).

1. Bruce, P. G., Freunberger, S. A., Hardwick, L. J. & Tarascon, J.-M. Li-O_2 and Li-S batteries with high energy storage. *Nat. Mater.* **11**, 19–29 (2012).
2. Evers, S. & Nazar, L. F. New Approaches for high energy density lithium–sulfur battery cathodes. *Acc. Chem. Res.* **46**, 1135–1143 (2012).
3. Ji, X., Lee, K. T. & Nazar, L. F. A highly ordered nanostructured carbon-sulphur cathode for lithium-sulphur batteries. *Nat. Mater.* **8**, 500–506 (2009).
4. Yin, Y., Xin, S., Guo, Y. & Wan, L. Lithium–sulfur batteries: Electrochemistry, materials, and prospects. *Angew. Chem. Int. Ed.* **52**, 13186–13200 (2013).
5. Lee, J. T. *et al.* Sulfur-infiltrated micro- and mesoporous silicon carbide-derived carbon cathode for high-performance lithium sulfur batteries. *Adv. Mater.* **25**, 4573–4579 (2013).
6. Lu, S., Chen, Y., Wu, X., Wang, Z. & Li, Y. Three-dimensional sulfur/graphene multifunctional hybrid sponges for lithium-sulfur batteries with large areal mass loading. *Sci. Rep.* **4**, 4629 (2014).
7. Chen, H. *et al.* Ultrafine sulfur nanoparticles in conducting polymer shell as cathode materials for high performance lithium/sulfur batteries. *Sci. Rep.* **3**, 1910 (2013).
8. Cheng, X. *et al.* Polysulfide shuttle control: Towards a lithium-sulfur battery with superior capacity performance up to 1000 cycles by matching the sulfur/electrolyte loading. *J. Power Sources* **253**, 263–268 (2014).
9. Suo, L., Hu, Y., Li, H., Armand, M. & Chen, L. A new class of Solvent-in-Salt electrolyte for high-energy rechargeable metallic lithium batteries. *Nat. Commun.* **4**, 1481 (2013).
10. Xin, S. *et al.* Smaller sulfur molecules promise better lithium–sulfur batteries. *J. Am. Chem. Soc.* **134**, 18510–18513 (2012).
11. Fu, Y., Su, Y. & Manthiram, A. Li_2S-carbon sandwiched electrodes with superior performance for lithium-sulfur batteries. *Adv. Energy Mater.* DOI: 10.1002/aenm.201300655 (2014).
12. Yang, Z. *et al.* In situ synthesis of lithium sulfide-carbon composites as cathode materials for rechargeable lithium batteries. *J. Mater. Chem. A* **1**, 1433–1440 (2013).
13. Han, K. *et al.* Li_2S-reduced graphene oxide nanocomposites as cathode material for lithium sulfur batteries. *J. Power Sources* **251**, 331–337 (2014).
14. Seh, Z. W. *et al.* Facile synthesis of Li_2S-polypyrrole composite structures for high-performance Li_2S cathodes. *Energy Environ. Sci.* **7**, 672–676 (2014).
15. Zheng, S. *et al.* In Situ formed lithium sulfide/microporous carbon cathodes for lithium-ion batteries. *ACS Nano* **7**, 10995–11003 (2013).
16. Nan, C. *et al.* Durable carbon-coated Li_2S core-shell spheres for high performance lithium/sulfur cells.J. Am. *Chem. Soc.* **136**, 4659–4663 (2014).
17. Yang, Y. *et al.* New nanostructured Li_2S/silicon rechargeable battery with high specific energy. *Nano Lett.* **10**, 1486–1491 (2010).
18. Hassoun, J. & Scrosati, B. A high-performance polymer tin sulfur lithium ion battery. *Angew. Chem. Int. Ed.* **49**, 2371–2374 (2010).
19. Yang, Y. *et al.* High-capacity micrometer-sized Li_2S particles as cathode materials for advanced rechargeable lithium-ion batteries. *J. Am. Chem. Soc.* **134**, 15387–15394 (2012).
20. Seh, Z. W. *et al.* High-capacity Li_2S-graphene oxide composite cathodes with stable cycling performance. *Chem. Sci.* **5**, 1369–1400 (2014).
21. Lin, Z., Liu, Z., Dudney, N. J. & Liang, C. Lithium superionic sulfide cathode for all-solid lithium–sulfur batteries. *ACS Nano* **7**, 2829–2833 (2013).
22. Fu, Y., Zu, C. & Manthiram, A. In situ-formed Li_2S in lithiated graphite electrodes for lithium–sulfur batteries. *J. Am. Chem. Soc.* **135**, 18044–18047 (2013).
23. Cai, K., Song, M.-K., Cairns, E. J. & Zhang, Y. Nanostructured Li_2S–C composites as cathode material for high-energy lithium/sulfur batteries. *Nano Lett.* **12**, 6474–6479 (2012).
24. Maier, J. Nanoionics: ion transport and electrochemical storage in confined systems. *Nat. Mater.* **4**, 805–815 (2005).
25. Duan, W. *et al.* $Li_3V_2(PO_4)_3$@C core-shell nanocomposite as a superior cathode material for lithium-ion batteries. *Nanoscale* **5**, 6485–6490 (2013).
26. Hu, Z. *et al.* Li_2MnSiO_4@C nanocomposite as a high-capacity cathode material for Li-ion batteries. *J. Mater. Chem. A* **1**, 12650–12656 (2013).
27. Chen, J. & Cheng, F. Combination of lightweight elements and nanostructured materials for batteries. *Acc. Chem. Res.* **42**, 713–723 (2009).
28. Wang, Y., Li, H., He, P., Hosono, E. & Zhou, H. Nano active materials for lithium-ion batteries. *Nanoscale* **2**, 1294–1305 (2010).
29. Zhang, K., Zhao, Q., Tao, Z. & Chen, J. Composite of sulfur impregnated in porous hollow carbon spheres as the cathode of Li-S batteries with high performance. *Nano Res.* **6**, 38–46 (2013).
30. Andrikopoulos, K. S., Kalampounias, A. G., Falagara, O. & Yannopoulos, S. N. The glassy and supercooled state of elemental sulfur: Vibrational modes, structure metastability, and polymer content. *J. Chem. Phys.* **139**, 124501 (2013).
31. Yang, Y., Zheng, G. & Cui, Y. Nanostructured sulfur cathodes. *Chem. Soc. Rev.* **42**, 3018–3032 (2013).
32. Wang, L. *et al.* Porous CuO nanowires as the anode of rechargeable Na-ion batteries. *Nano Res.* **7**, 199–208 (2013).
33. Gao, H., Hu, Z., Zhang, K., Cheng, F. & Chen, J. Intergrown $Li_2FeSiO_4 \cdot LiFePO_4$-C nanocomposites as high-capacity cathode materials for lithium-ion batteries. *Chem. Commun.* **49**, 3040–3042 (2013).
34. Ma, H., Zhang, S., Ji, W., Tao, Z. & Chen, J. α-CuV_2O_6 nanowires: hydrothermal synthesis and primary lithium battery application. *J. Am. Chem. Soc.* **130**, 5361–5367 (2008).
35. Reale, P. *et al.* A safe, low-cost, and sustainable lithium-ion polymer battery. *J. Electrochem. Soc.* **151**, A2138–A2142 (2004).
36. Hassoun, J., Panero, S., Reale, P. & Scrosati, B. A new, safe, high-rate and high-energy polymer lithium-ion battery. *Adv. Mater.* **21**, 4807–4810 (2009).
37. Wang, S. *et al.* Organic $Li_4C_8H_2O_6$ nanosheets for lithium-ion batteries. *Nano Lett.* **13**, 4404–4409 (2013).
38. Staudenmaier, L. Verfahren zur darstellung der graphitsaure. *Ber. Dtsch. Chem. Ges.* **31**, 1481–1487 (1898).

Acknowledgments

This work was supported by the Programs of National 973 (2011CB935900), NSFC (21231005), MOE (B12015, 113016A, and IRT13R30), and Fundamental Research Funds for the Central Universities.

Author contributions

K.Z. and L.W. designed the experiments, synthesized the materials, and performed the characterization. K.Z., L.W., and Z.H. carried out the electrochemical tests. All authors contributed to results analysis and manuscript preparation. J.C. and F.C. supervised and directed the study.

Additional information

Supplementary information accompanies this paper at http://www.nature.com/scientificreports

Competing financial interests: The authors declare no competing financial interests.

How to cite this article: Zhang, K., Wang, L., Hu, Z., Cheng, F. & Chen, J. Ultrasmall Li_2S Nanoparticles Anchored in Graphene Nanosheets for High-Energy Lithium-Ion Batteries. *Sci. Rep.* **4**, 6467; DOI:10.1038/srep06467 (2014).